E. CARLINO*   V. GRILLO*

# ATOMIC RESOLUTION STEM-HAADF IMAGING IN THE STUDY OF INTERFACES

## BADANIA GRANIC ROZDZIAŁU W SKALI ATOMOWEJ Z WYKORZYSTANIEM TECHNIKI STEM-HAADF

Current efforts to develop nanostructured materials and devices are stimulating the implementation of new experimental probes of the structure and chemical composition of solids on the atomic scale. High-resolution transmission electron microscopy (HRTEM) has been widely used in the last decades to study the structure and the properties of materials at the highest spatial resolution. More recently high angle annular dark field (HAADF) scanning transmission electron microscopy (STEM) imaging has demonstrated sub-Angstrom resolution together with high sensitivity to the chemical composition of the material allowing to study both the structure and the chemistry of interfaces at atomic resolution without the uncertainty related to the phase problem in HRTEM. Here, basic principles of HAADF imaging will be illustrated together with recent applications to the study at atomic resolution of interfaces of materials. It will be shown how HAADF can be used to probe the distribution of guest chemical species in a host matrix. Furthermore, a new approach to the simulation of HAADF images will be introduced together with a new approach to the determination of important experimental parameters as defocus values and specimen thickness.

*Keywords*: TEM, HRTEM, STEM, HAADF, atomic resolution imaging, simulation

Obecna aktywność w zakresie rozwoju nanomateriałów stymuluje konieczność opracowania nowych technik badawczych umożliwiających ich charakterystykę mikrostruktury i składu chemicznego w skali atomowej. Dotychczas, tj. w zakresie kilku ostatnich dziesięcioleci, do charakterystki mikrostruktury materiałów z najwyższa przestrzenna zdolnością rozdzielczą wykorzystywana była mikroskopia skaningowa, która w trybie tzw. wysoko-kątowego ciemnego pola (HAADF) umożliwia zarówno obserwacje mikrostruktury jak i charakterystykę chemiczną z rozdzielczością rzędu jednego Angstrema i to bez obciążenia problemem delokalizacji właściwym klasycznej mikroskopii wysokorozdzielczej.

W bieżącym opracowaniu zostaną zaprezentowane podstawowe zasady prowadzenia obserwacji mikroskopii transmisyjno-skaningowej z wykorzystaniem trybu HAADF oraz przedstawione przykzastosowania tej techniki do obserwacji granic między-fazowych w skali atomowej. W szczególności opisany sposób wykorzystania HAADF do analizy rozkładu domieszek w osnowie kryształu. Następnie, przedstawiony zostanie nowy sposób modelowania obrazów HAADF umożliwiający wyznaczenie takich parametrów jak grubości cienkiej folii oraz wartości odstępstwa od warunków minimalnego kontrastu.

## 1. Introduction

Transmission electron microscopy (TEM) has demonstrated in the last decades how the comprehension of the properties of materials for technological application needs of the knowledge of their structure and chemistry at the highest spatial resolution. More recently, nanoscience has given further incentive to develop new reliable tools to probe the properties of materials at the atomic scale. High resolution TEM (HRTEM) has been widely applied to study the structure and the chemistry of materials at atomic resolution [1, 2, 3]. HRTEM images are highly sensitive to the crystal structure and to the chemistry of the specimen but image contrast are also highly sensitive to the imaging condition like defocus value, spatial and temporal coherency of the electron probe and specimen thickness. Furthermore, HRTEM images of strained materials can produce wrong interpretation if not compared with a reliable model able to take into account the effect of thinning process during TEM specimen preparation. In fact, the very low thickness necessary for TEM experiments produces a modification of the strain fields of the specimen, due to the relevant elastic stress relaxation, changing in a complex

way the contrast of TEM [4] and HRTEM images [5]. As a result the HRTEM data of unknown structures have to be compared to the relevant simulation to understand the real specimen structure and cannot certainly be interpreted intuitively from the appearance of the image contrast. As an example, even the position of the atomic column in the structure cannot be easily interpreted from the presence of white or black dots in the image as the contrast features are a not straightforward combination of objective lens defocus values and specimen thickness, as shown in Figure 1.
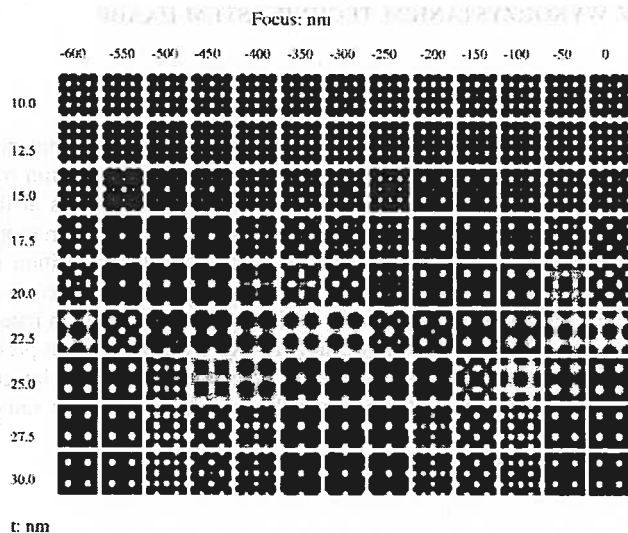


Fig. 1. Through focus/trough thickness map for HRTEM images calculated for GaAs in < 001 > zone axis. It results that the bright or dark spots are not necessarily related to the position of the atomic columns in the specimen

Another approach to the direct imaging of crystal atomic column projected along precise crystallographic direction can be achieved by a methodology developed more recently in scanning transmission electron microscopy (STEM) and named high angle annular dark field (HAADF) imaging [6]. This approach in many cases produces atomic resolution results with a direct and intuitive interpretability, due to the incoherent process at the base of the relevant image formation. Furthermore, HAADF images contain detailed information on the chemistry of the specimens. In fact, due to the high sensitivity to the chemistry of the specimen, HAADF imaging is also known as Z-contrast imaging. A big advantage of HAADF imaging, with respect to coherent imaging, is its relatively low dependence on specimen thickness and defocus value thus producing images in which white dots represents, for a wide range of thickness and defocus, the position of the atomic columns, seen in a certain projection, as demonstrated by the simulation shown in Figure 2.
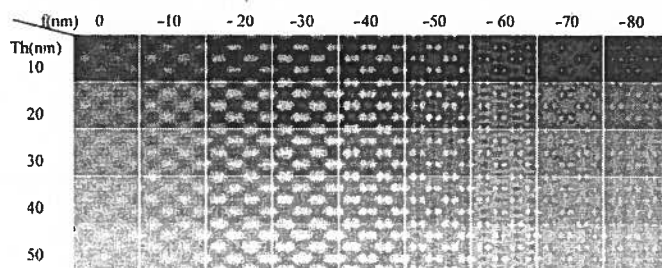


Fig. 2. Through focus/through thickness for HAADF images calculated for GaAs in < 110 > zone axis. It is worth noting that in a wide range of thickness and defocus values the position of the projected atomic column do not change artificially

Furthermore, the proper choice of the experimental conditions allows to obtain experimental results from strained materials, largely independent of long range strain fields [7] allowing to derive detailed chemical information at atomic resolution even without image simulation [8]. Certainly, as will be shown below, more detailed and quantitative information can be obtained coupling HAADF imaging with the relevant computer simulation [9, 10]. Another interesting feature of HAADF is related to the geometry of the experiments in STEM. As the image is acquired by scanning a small electron probe, of the order of 0.1 nm, across the specimen, the imaging can be easily coupled to energy dispersive x-ray spectroscopy (EDS), or electron energy loss spectroscopy (EELS), simply by stopping the electron probe on an atomic column, or along a line, or in an area of interest, thus achieving atomic resolution information related to the EDS or EELS spectra with the highest spatial accuracy [11, 12]. STEM HAADF imaging at the beginning of its introduction in 1990 [6] had a relatively small diffusion probably due to the need of dedicated STEM equipment having a relatively smaller diffusion with respect TEM equipment. Nevertheless, the interesting results achieved and, more recently, the development of TEM microscope with field emission guns of last generation, equipped with STEM attachments, capable of performances comparable with the dedicated STEM instruments, paved the way to a rapid increase of the application of HAADF imaging in many problems of materials science. The scenario is even more attractive for HAADF imaging due to the recent introduction of spherical aberration corrected dedicated microscopes able to image the structure at sub Å scale and close to the ultimate resolution limit [8]. Here, it will be shown the basic principles of HAADF imaging together with recent application aimed to the knowledge of the structure and chemistry of the specimens at atomic resolution. The paper is organized as follows: in paragraph II the image formation in HAADF is introduced; in par. III the experimental apparatus is described; in par IV a new approach

to parallel computing of HAADF images is introduced, in par. V it is shown how Z-contrast imaging can be used to gauge at atomic resolution the distribution of a guest chemical species in a host matrix; par VI reports on a novel approach to determine the defocus value and the specimen thickness from a HAADF experiment and finally in par. VII the conclusions are drawn.

## 2. HAADF image formation

The intensity in a HAADF image is given by

$$I(r) = O(r)*P^2(r), \tag{1}$$

where $O(r)$ is the object function and $P^2(r)$ is the resolution function [9]. In an atomic resolution Z-contrast STEM experiment the available resolution is hence due to the size of the object function, $O(r)$, convoluted with the size of the resolution function, $P^2(r)$, where the latter is the size of the electron beam scanned on the specimen [9]. The image is hence formed incoherently with negligible phase contrast influence. The combined effect of the use of an annular STEM detector with a collection angle larger than 80 mrad and thermal diffuse scattering, relevant at high scattering angle [14], produces an image in which the main contribution is given by the 1s columnar states [15]. The 1s columnar Bloch states are ideal if the aim is to solve the position of the atomic columns as they are less dispersed around the positions of the atomic columns with a full-width-at-half-maximum (FWHM), for example for GaAs in < 110 > zone axis, of only 0.06–0.08 nm [11]. Emphasizing the 1s columnar states provides the best picture and the ultimate resolution achievable in an atomically resolved TEM/STEM experiment. The HAADF image formation process is summarized in Figure 3.

The use of a field emission gun allows one to obtain small and highly coherent probes. $0.43\,C_s^{1/4}\lambda^{3/4}$ gives the smallest size of an electron beam achievable in a STEM [16] where $C_s$ is the spherical aberration coefficient of the objective lens and $\lambda$ is the electron wavelength. A 200 KV accelerating voltage commercial TEM system with STEM attachment, $C_s = 0.5$ mm and field emission gun source has a theoretical limit for the spatial resolution in Z-contrast of 0.126 nm, well below the spacing of the GaAs dumbbells atoms in the [110] projection, and the resolution of 0.19 nm achievable in phase contrast at the optimum defocus. Hence, incoherent imaging at optimum defocus gives higher resolution than HRTEM at optimum defocus [16]. Furthermore, the intensity in a HAADF image is strongly dependent on the average atomic number of the chemical species in the atomic columns. In fact, the object function convoluted with the annular detector is given approximately by [17]:
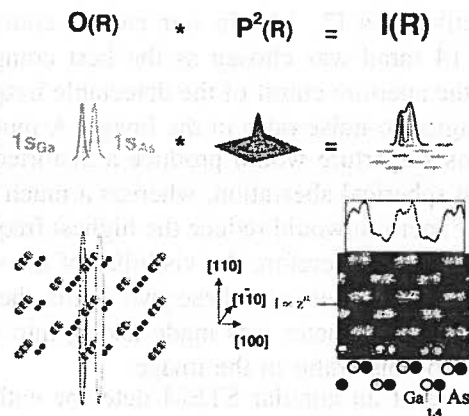


Fig. 3. Image formation scheme for HAADF image. The image is formed incoherently as it is formed by the convolution of the object function with the resolution function. It should be noted that the intensity in each projected atomic columns is simply and strongly related to the average atomic number in the column

$$O(R)=\sigma^2 V^2(R).$$

Where $\sigma$ is the interaction constant m/h², m is the relativist mass of the electron and $V(R)$ is the projected potential [18]. Hence, for high scattering angles, the intensity of the bright spots in the images, corresponding to the position of the projected atomic columns, is proportional to the square of the average projected potential and hence to the square of the atomic number of the chemical species inside the projected atomic column. An accurate calculation of the Bloch states intensity in the framework of a purely dynamical theory shows that the quadratic dependence of $V(R)$ is a good approximation for any chemical species. Moreover, for quantitative results, the right value of the exponent should be accurately calculated for the chemical specie to be quantitatively analyzed in order to avoid large errors [11].

## 3. Experimental

HAADF experiments, shown in the following, were performed at room temperature using a JEOL 2010F UHR TEM/STEM field-emission gun electron microscope, operating at 200 kV with a measured spherical aberration coefficient $C_s$ of 0.47 ± 0.01 mm. Therefore the interpretable resolution limit in HRTEM was 1.9 Å [2].

For Z-contrast imaging, the STEM attachment was equipped with a YAP HAADF detector. The theoretical resolution achievable in Z-contrast mode with the available electron optics was 0.126 nm [19, 20]. All Z-contrast micrographs were recorded with a collection angle $84 \leqslant 2\vartheta \leqslant 224$ mrad. The convergence angle, and hence the optimum aperture of the condenser, is related to the spherical aberration coefficient of the pre-field of

the objective lens [7, 14]. In our case a convergence angle of 14 mrad was chosen as the best compromise between the aperture cutoff of the detectable frequencies and the signal-to-noise ratio in the image. A much larger condenser aperture would produce a distorted image due to the spherical aberration, whereas a much smaller condenser aperture would reduce the highest frequencies in the images and therefore the visibility of the smallest lattice spacing. In between these two limits the choice of the aperture diameter was made taking into account the signal-to-noise ratio in the image.

The use of an annular STEM detector with a collection angle larger than about 80 mrad allows acquisition of mainly incoherent electrons, since thermal diffuse scattering dominates at high scattering angles [14].

Specimen preparation is an important issue in any TEM/STEM experiments so special care has been devoted to the preparation of the samples used to quantify the distribution of Si in GaAs matrix, which will be shown in the next paragraph as an example of the capability of HAADF to quantify chemical species in a host matrix. There are some peculiarities in the specimen preparation for quantitative atomic resolution profiling of chemical species by STEM HAADF as the surfaces of the thin films have even more importance than usual. With this respect, three points are of particular importance: the surface has to be the smoothest possible with no clustering, the amorphous layer due to the ion milling process has to be the thinnest possible and the hydrocarbon contaminants have to be as low as possible to avoid contamination pile-up due to the highly focused probe used in HAADF experiments. The specimens were prepared in {110} cross section geometry. Milling conditions and geometry were chosen in order to minimize differential sputtering between substrate and epilayer [21]. In particular two ion-guns were used – one for each side of the TEM specimen – in order to avoid re-deposition of sputtered material on the opposite surface. Furthermore, the use of a shallow milling angle and high Z-number ions reduce the dependence of the sputtering process on the specimen atomic number. In this case, the milling geometry was chosen in order to have the ion beam direction forming an angle of 4° relative to the {110} plane. Such precautions were employed together with a discontinuous milling process during rotation of the specimen holder. In particular, the guns were switched on only when the ion beams where within ± 30° of the direction normal to the Ga(Si)As-GaAs interface. Hence, no sputtering was allowed when the ion beams were parallel to heterostructure interface, as such geometry is known to enhance preferential sputtering of the interface region. The milling procedure was performed by using Xe+ ions, with energy of 4.5 keV for the initial part of the milling process, and progressively reduced down to 2KeV up

to the formation of a small hole. Then, to remove the layers damaged by the high-energy ions, the specimen were ion milled by using hot cathode ion guns specially designed to operate down to 200 V. Finally, the specimen and specimen holder were treated in low-energy, high frequency plasma of argon and oxygen to remove hydrocarbon contamination, prior to be inserted in the electron microscope vacuum.

## 4. Improved codes for the calculation of HAADF image contrast

In spite of the intuitive interpretability of the HAADF image contrast, a large amount of computer work in both simulation and data analysis is necessary to extract quantitatively most of the information contained in HAADF images. As an example, image simulations are necessary to study the parametric dependence of HAADF images on experimental quantities to establish a chemical quantification methodology [10]. Unfortunately, an accurate simulation of HAADF image contrast requires very long computing time, orders of magnitude longer with respect to the time necessary for the relevant phase contrast high-resolution transmission electron microscopy contrast simulation [22]. Nevertheless, it is possible to optimise the computer codes necessary for HAADF image simulation in order to reduce the computer time necessary to obtain precise results.

The simulation of HAADF images has been approached by both multi-slice [23, 24] and Bloch wave methods [25, 26, 27]. State of the art Bloch wave based methods present mainly the advantage of being relatively fast in the simulation of periodic structures. Additionally, as for example demonstrated by a recent article from Peng [28], some interesting insight of the image formation can be qualitatively better understood by a detailed analysis of the excited Bloch wave at the crystal surface.

Nevertheless, if a complex super-cell is necessary to describe the material under study or in any case in which a great accuracy of the results is required, the best method for HAADF image simulation is the multi-slice simulation along with frozen phonon approximation [29]. As convincingly demonstrated by many authors [30] the most important contribution to HAADF image intensity arises from Thermal Diffuse Scattering (TDS): the thermal random displacements of the atoms, from their equilibrium position inside the crystal, induce local deviation from the exact Bragg condition. The electrons are therefore partly diffused at a wide range of angles outside the Bragg peaks. For its nature this non-periodic scattering effect cannot easily fit in a typical periodicity based algorithm as the Bloch wave. One of the major weaknesses of many Bloch wave approaches is that dif-

fuse scattering does not indeed appear from calculation but has to be included by *"ad hoc"* phenomenological potentials [26, 27]. For this reason it is, for example, difficult to account for the dynamical re-scattering of the diffused wave [26].

On the contrary, the multi-slice method in the frozen phonon (FP) approximation naturally includes all phonon effects: the frozen phonon approach is based on the assumption that the high-energy electrons are so fast that each electron sees a snapshot of the atomic thermal movement. The calculated intensity is therefore the incoherent superposition of the images formed for each atomic configuration in the range of positions given by the Debye-Waller factors. According to our test simulations, and in agreement with literature [29, 31, 32], 20 configurations are necessary to converge to a precision better than 2% in simulating HAADF image contrast. Furthermore, if some symmetry in the final image is present, the number of configurations can be reduced [22]. Hence, multi-slice simulation must be repeated for each atomic configuration and for each point of the image. It can be easily seen that as soon as the sample thickness reaches realistic values for a comparison with the experiments, or the sampling requirements become more stringent to obtain a best accuracy in simulations, the computing time tend to become very large, of the order of hundreds hours of CPU time. Some improvement of the codes can be made reducing of orders of magnitude the computing time. The initial implementation of our simulation was largely based on the well-established work of Kirkland [24] who developed several routines to generate potential slices, perform multislice simulations and store results. Hence, the first step is to reorganize these routines and add the possibility to perform integration over the different FP configuration. The code was then optimized to reduce the CPU computing time. This operation does not change the structure of the code but rather its transcription in machine language. Optimization was performed by means of:

1) Use of system dependent compilation options;

2) Reorganization of lengthy loops accessing large 2D data array;

3) Removing, wherever possible, redundant loop;

4) Avoiding the use of any intermediate hard disk access during simulations.

In most calculations, after this optimization, the code required about half of the initial CPU time.

The largest improvement has been, however, the use of a parallel code that permitted to strongly reduce the computing time. Indeed, the calculation for HAADF image simulation based on multi-slice approach has a logical structure particularly suitable for parallelisation. The simulation is performed independently for each position of the probe on the specimen structure and repeated for each atomic configuration to take into account the thermal diffuse scattering in the FP approximation.

This first aspect has been here tackled in a parallelisation. This "embarrassing parallel" scheme allows to adopting a form of parallelism based on the MPI message passing library and its free implementation MPICH [33]. MPICH message passing protocol permits to send arrays of data between different CPU running the same program. This permits to run the simulation on different machines and collect the final results. At the beginning of the simulation the image is divided into different sets of non-consecutive pixels, which are assigned to each CPU. Each CPU fills the assigned part of the matrix with the simulation results after averaging over the different configurations. When all CPUs have completed their jobs, data are passed by means of the MPI protocols to a single processor that recomposes as a puzzle the final image. This scheme has the noticeable advantage of being scalable up to Nx x Ny (the number of pixels of the final image). The smallest sampling reasonably usable consists of about 200 pixels. The code is scalable up to a very large number of CPU in many computer cluster of common use. Moreover the number of pixels can be often chosen in order to be a multiple of the number of CPU. This permits a more efficient distribution of the calculation among the different CPUs and a reduction of the CPU time in our calculation of a factor 30 [34, 35]. It is worth noting that a reduction of two orders of magnitude in the HAADF image simulation can be reached on clusters of computers widely accessible.

## 5. HAADF to measure the profile of Si in GaAs matrix

In order to give a quantitative meaning to the HAADF contrast, different aspects of the HAADF image can be considered: these are for example the intensity at a maximum on an atomic position, or the area in a unit cell, or the shape of the dumbbell [22].

In this work we chose to use the information contained in laterally averaged intensity profiles. This permits to have a good signal to noise ratio while a relatively small influence of the drift induced distortion of the image was evidenced.

In order to assign chemical information to the experimental HAADF intensity, it is necessary to perform a set of simulations defining in a proper way the model structure; the average over the simulated unit cell can be directly compared to the laterally averaged profile.

There are two points to be considered in details to simulate the HAADF images: first how to realize the structure whenever an alloy is considered; second,

the parametric expression describing the dependence of the intensity on molar fraction of the different chemical species [10]. The partial occupation concept is largely used in simulating an alloy in HRTEM images with reliable results. In fact, in the simulations it is possible to account for a partial substitution of a species with another, as in a solid alloys, by simply considering a partial occupation coefficient x. This is also known in solid-state physics as "virtual crystal approximation". The potential in each point becomes therefore simply a weighted linear combination of the potential of each species. The virtual crystal approximation can be applied in this scheme for conventional simulation of HRTEM results, and indeed it is largely applied, producing reliable results. The same kind of approach can yield formation of artifacts in frozen phonon simulations of HAADF images due to the incoherent nature of the HAADF image. In fact, while the electron probe is propagating along the crystal column, it interacts with the potential of each atom and the shape of such potential influences the results. To take into account the interaction with phonons along the direction of propagation, the atoms are displaced from their rest position and the final results are given by considering an appropriate configuration of atoms to reproduce the effect of the scattering with a phonon. This is at the origin of the so-called frozen-phonon approximation above introduced. The approach works very well if, in a certain position, there is one atom but could fail if the position is occupied by $x_A\%$ of the potential of atom A and $(1-x_A)\%$ of the potential of atom B. A possible solution to this inconvenient could be to displace both the weighted potentials in the same direction with a proper, not obvious, Debye-Waller factor or to consider the different configuration obtainable and to average on the all relevant results [10]. The choice of averaging on different configurations can be also used to consider the influence of the position of atoms of different species, located in the same atomic column, not equivalent to other positions [10]. Indeed the choice of averaging on all the possible atomic configurations $\bar{I} = \frac{\sum\limits_{i=config.} I_i}{N_{config}}$ can overcame this problem but intrinsically produces a loss of accuracy in the simulation that can be calculated and considered as one of the component of the "experimental" error in the measurement of the chemical composition by HAADF [10].

The second step to be considered is the interpolating expression to be used to derive the specimen composition from the intensity in HAADF; with this respect it has been shown that for Si buried in GaAs [10] there is a quasi-linear dependence of the HAADF image intensity on the Si content but it is worthwhile to remark, that deviation from linearity can be found for different alloys [36].

However, different other parameters can influence the contrast for a given alloy and their effects require a brief discussion.

The defocus is usually considered an important parameter. However, experimentally, conditions close to Scherzer defocus are most frequently used. As long as the probe remains in channeling conditions the residual variation from this values have a much lower effect mainly because we are considering wave-function redistributions within the unit cell. Such effects disappear in the calculation of the average intensity. For this reason in our analysis it is of lesser importance to perform a probe deconvolution as in the approach suggested i.e. by K . W a t a n a b e et al. [37].

The thickness of the TEM specimen is another parameter influencing the chemical contrast. The specimen thickness can be evaluated by convergent beam electron diffraction or by electron energy loss spectroscopy, however it would be ideal to be able to extract thickness directly from HAADF images. This is what attempted Y a m a z a k i et al. [38] by an overall image fitting of the contrast but a more direct thickness evaluation would be also desirable. One of these alternative methods recently under development is described in the next session.

However for the present discussion of the GaAsSi alloy the detailed knowledge about sample thickness is not crucial. Simulations show indeed that for Ga(As)Si alloy the contrast defined as:

$$C_{100\%} = \frac{I_{GaAs} - I_{SiAs}}{I_{GaAs}}$$

is little varying with thickness as it decreases from 0.30 to 0.26 for increasing thickness from 10nm to 40nm. To a first approximation it can be assumed it is constant with an absolute error of about 0.02, namely $C_{100\%} = 0.28 \pm 0.02$, this error can be larger for larger or lower thickness but it is a good reference as experimentally it is easy to perform an HAADF experiment for a thickness within the considered range. Consequently the Si concentration x can be measured by using:

$$x = \frac{C_{measured}}{C_{100\%}}.$$

Where $C_{measured}$ is the experimental contrast defined as $\frac{I_{GaAs} - I_{SiGaAs}}{I_{GaAs}}$. Let us consider the experimental image in Figure 4.

Figure 4a shows a high magnification atomic resolution HAADF image of nominally one Si atomic layer buried in GaAs. Indeed, the Si atom are spread on several atomic planes and the content of Si on each atomic plane can be measured by HAADF imaging. The specimen has been grown by molecular beam epitaxy with exper-

imental parameters reported elsewhere [8]. It is worthwhile to remark how the image contrast, away from the Si-rich region, is homogeneous thus providing evidence for atomically flat specimen surfaces necessaries for reliable contrast quantification. A careful inspection of the elongated white dots in Fig. 4a allows one to distinguish the cation-anion columns seen projected onto the (110)
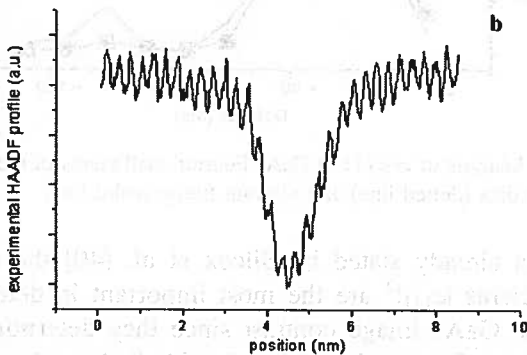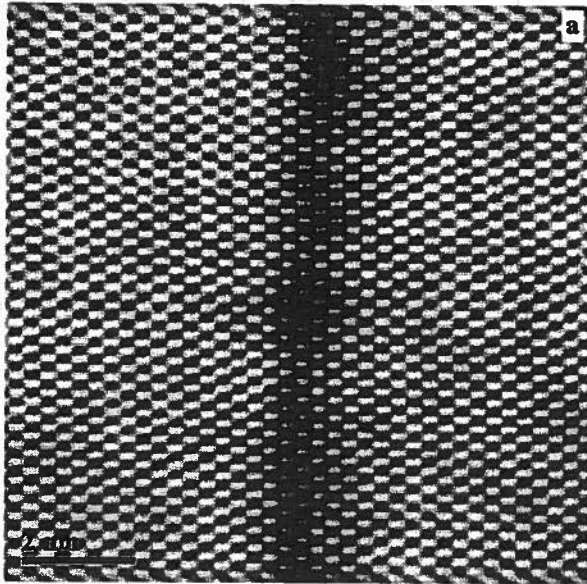


plane and spaced by 0.14 nm. In Fig. 4b the experimental image intensity in Fig. 4a is plotted as a function of the distance from the interface. The higher peaks, 1.5 nm away from the minimum in the intensity profile, reflect the higher atomic number of the III-V species. The im-

age intensity decreases in going from the GaAs region toward the metallurgical Si-GaAs interface due to the presence of Si in the atomic columns.

To evaluate the image contrast the detector background has been subtracted and the intensity value has been normalized to the GaAs regions on both sides of the dark Si-rich region. Appling the expression $x = \frac{C_{measured}}{C_{100\%}}$, the Si distribution can be obtained as shown in Fig. 5 by the red bars.
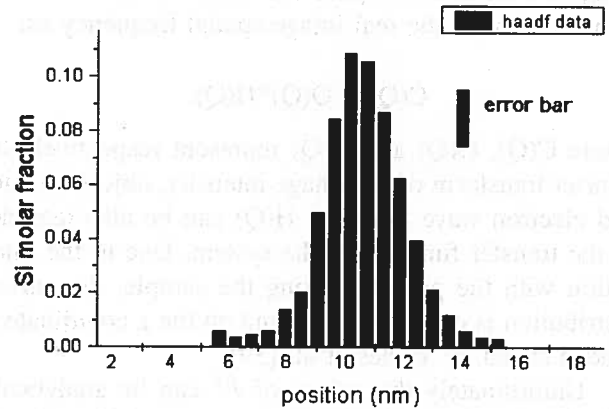


Fig. 5. Si profile as measured from HAADF image in figure 4

It worthwhile to remark the source of errors in the measurement: the first is related to the averaging procedure on the different atomic configurations in the columns, the second is related to the error in the defocus value, the third is due to the error on the specimen thickness. Also the effect of the hydrostatic strain has been simulated and considered in the quantification [10]. As a result this measure of the Si profile in GaAs is affected by an error of ±2%, which is still very good if we consider the accuracy in the spatial resolution achieved with this approach.

## 6. Defocus and thickness determination by focal series analysis

Whereas not crucial in the above example, the knowledge of the defocus and thickness can considerably reduce the uncertainty in the chemical quantification. However one of the problems that weaken the direct image fitting approach to thickness and defocus determination is that these techniques rely on the analysis of single image. In this case the estimation is statistically less meaningful while more sets of experimental conditions could give rise to a good fitting, because of local minima in the likelihood function.

One of the promising alternative approaches is based on the use of a focal series with a range of defoci from

Fig. 4. a) Experimental atomic resolution HAADF image of nominally one monolayer of Si buried in GaAs matrix. The darker regions represent zones of lower high angle scattering of primary electrons due to the lower atomic number of Si with respect to the Ga and As. b) experimental image intensity in a) plotted as a function of distance from the interface. The higher peaks, 1.5 nm away from the minimum in the intensity profile, reflect the higher atomic number of the III-V species. The image intensity decreases in going from the GaAs region toward the metallurgical Si-GaAs interface due to the presence of Si in the atomic columns

0 to − 100nm. The analysis is performed in the Fourier space where the main contrast features are contained in a few coefficients: for a relatively large range of thickness the dependence of these factors on defocus can be fitted to the theoretical dependence of a non-scattering probe: the value of defocus can be extracted as free parameter of this fitting. In addition this analysis can provide information about the sample thickness.

To understand the detail of this procedure it is necessary to start from the equ. 1 of the intensity in HAADF image. In the Fourier space the same relation is written as a function of the real image spatial frequency as:

$$C(Q) = O(Q)*H(Q),$$

where $C(Q)$, $O(Q)$ and $H(Q)$ represent respectively the Fourier transform of the image intensity, object function and electron wave function. $H(Q)$ can be also regarded as the transfer function of the system. Due to the interaction with the potential along the sample, the current distribution is expected to depend on the z coordinate as indeed stated by Voyles et al. [39].

Unfortunately the values of $P^2$ can be analytically calculated only for the impinging probe before the interaction with the sample. In this case the probe can be written as:

$$P^2(\vec{r}_{probe} - \vec{r}, 0, f) = \left| \int_{|\vec{K}|=0}^{|\vec{K}|_{max}} e^{-i\chi(k,f)} e^{i\vec{k}(\vec{r}_{probe}-\vec{r})} d^2\vec{k} \right|^2 , \quad (2)$$

where $\vec{r}_{probe}$ and $\vec{r}$ are the position of the center of the probe and of a generic observation point, both expressed in x,y coordinates of the sample plane while:

$$\chi(\vec{k}) = \pi\lambda k^2 (0.5 C_S \lambda^2 k^2 + f) \quad (3)$$

k is the wave-vector, $\lambda$ is the electron wavelength $C_s$ and $f$ are the objective lens spherical aberration coefficient and defocus with the convention that under focus values are negative. In a general case, however, for z > 0 the shape of the probe cannot be analytically calculated and some modification of its shape are expected. Nevertheless the method relies on the fact that the overall dependence of the probe on defocus is maintained for a quite large range of thickness. In the following the method will be applied to the case study of GaAs (Fig. 6 and Fig. 7).

The uppermost solid curve of Fig. 6, in particular, represents the dependence on defocus of the impinging probe Fourier coefficients at the spatial frequency $|Q| = 0.31$ nm$^{-1}$ (simulation has been performed for a Cs value of 0.5 and accelerating voltage of 200KeV) this

is the frequency of the <111> periodicities in a GaAs cell.
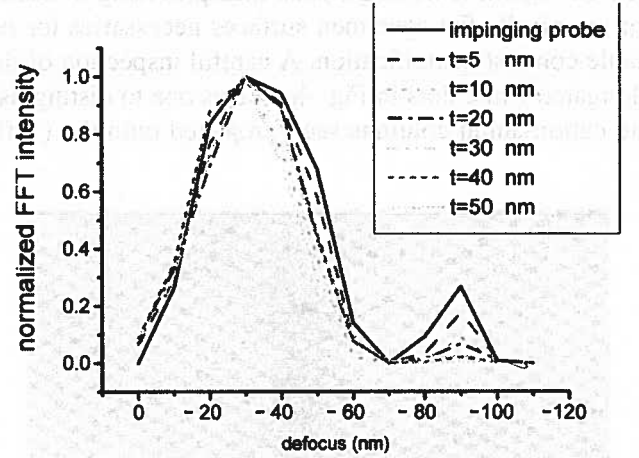


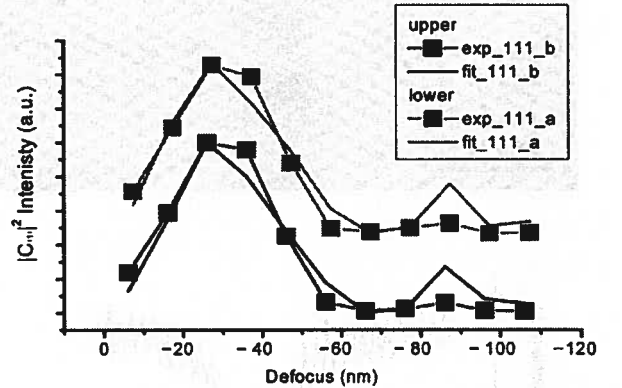Fig. 6. $|c_{111}|^2$ GaAs Fourier coefficient vs. defocus for different thickness



Fig. 7. Analysis of $c(<111>)$ GaAs Fourier coefficients of the experimental data (dotted line) and relevant fitting (solid line)

As already stated by Silcox et al. [40] the image coefficients $|c_{111}|^2$ are the most important in determining the GaAs image contrast since they determine the presence of the cation-anion dumbbell. Its value is related to the sum of the intensities of the two peaks in the dumbbell. On the contrary the $|c_{200}|^2$ delivers the information on the difference in HAADF intensity between the two atomic column in the dumbbell. It can be demonstrated that in the case of GaAs the most suitable Fourier coefficient for this analysis is the $|c_{111}|^2$ as shows a lower dependence on thickness [41]. A closer inspection of Fig. 6 reveals the peculiar behavior expected for the HAADF image: $|c_{111}|^2$ shows a plateau around the maximum at the Scherzer defocus and a characteristic dip appears for a defocus close to 70 nm while the most prominent secondary maximum appears for a defocus close to 90 nm.

This observation on the impinging probe coefficient needs some correction if the interaction with the sample

is considered. To fully account for the probe-specimen interaction, a complete multislice simulation has been performed for the case of interest of a GaAs single cell in projection [110].

The remaining curves in Fig. 6 show the dependence of the probe Fourier coefficient on defocus for a typical focal series in the range of defocus from 0 to - 100 nm and for specimen thickness from 5 nm to 50 nm. These curves tend to resemble each other with the only difference that the peak at - 90 nm is strongly decreased for increasing thickness. This demonstrates that the dependence of the probe on defocus is, to large extent, retained at different thickness. The spurious differences at defoci far from Scherzer and in particular for f = - 90 nm are also quite important. The ratio of the two $|c_{111}|^2$ for f = - 40 nm and for - 90 nm decreases monotonically with thickness: a characteristic monotonic curve can be obtained that correlate such ratio to the thickness.

Experimentally, it is necessary to obtain a HAADF image defocus series with a known step, usually 5-10 nm.

Hence, images are Fourier transformed and a single periodicity is isolated by selecting a rectangle around the peak in the Fourier space. The intensity of the Fourier transform in the rectangle for each image is then stored in a profile and normalized to its maximum value normally corresponding to a point in the surrounding of the Scherzer defocus. A fitting procedure has to be applied using as a minimization potential of the following function

$$U(Q) = \sum_f \frac{\left\| C^*_{exp}(Q, f) - H^*_{teo}(Q, f) \right\|}{H^*_{teo}(Q, f)},$$

where the "*" indicates that the given quantities are normalized to their maxima.

This function represents the difference between the experimental profile and the transfer function at the given frequency Q for a non-interacting probe. The fitting program permits to extract as a free fitting parameter the initial defocus of the series and, consequently, the values of the defocus for each of the image in the series.

The complete methodology has been applied for comparison to the simulated images in order to evaluate the typical error on evaluations at different thickness. The deviation between the actual defocus and the fitting estimation was always better than 2nm that can be considered the intrinsic uncertainty of the method.

Once the best value of the defocus is known for all images the ratio $|c_{111}(-90nm)|^2 / |c_{111}(-40nm)|^2$ can be easily extracted. Hence, by using of the above mentioned calibration curve, it is possible to evaluate the thickness.

This method can be extended to the calculation of defocus and thickness for different structures with the sole caution to avoid the use of Fourier coefficients too sensible to little intensity variations between the different atomic columns [41].

Fig. 7 shows the experimental curves indicating the dependence of the two equivalent $|c_{111}|^2$ GaAs Fourier coefficients as a function of defocus. The figure shows also the best fitting with the model behavior as described in the previous sections. The agreement between model and experiment is good and this demonstrates the accuracy of the simulations. The spurious differences can be probably ascribed to some astigmatism [41]. The thickness evaluation yielded a value of about 23 ± 6 nm.

## 7. Conclusions

HAADF imaging is an extremely powerful tool now available together with the other tools already available by using a TEM. Here we illustrated some recent applications of HAADF imaging and new methodology to measure at atomic resolution the profile of guest chemical specie in a host crystal matrix together with a new approach to the simulation of HAADF images and new approaches to the measurement of important experimental parameter like defocus values and specimen thickness. Furthermore, as the mechanism behind the image formation in HAADF is strongly related to the phonon spectrum in the specimen, a detailed comprehension and simulation of the features of the HAADF images allows and will allow understanding important aspects of the materials properties so far not reachable. Furthermore, the accuracy obtainable by positioning the electron probe by using atomic resolution HAADF imaging is producing and will produce more spatially resolved energy dispersive x-ray spectroscopy and electron energy loss spectroscopy information on the chemistry, the electronic structure and the magnetic properties of the materials. More and more electron microscopy demonstrates to be a flexible and powerful tool to study the properties of the materials at the highest spatial resolution.

REFERENCES

[1] D. Van Dyck, *Electron Microscopy in Materials Science*, Eds P. G. Merli and M. Vittori Antisari, World Scientific, 257 (1992).

[2] J. C. H. Spence, *Experimental High-Resolution Electron Microscopy*, $2^n d$ Ed. Oxford University Press, Oxford, 87 (1988).

[3] E. Carlino, C. Giannini, L. Tapfer, M. Catalano, E. Tournié, Y.H. Zhang, K. H. Ploog, J. Appl. Phys. **78**, 2403 (1995).

32

[4] M. M. J. Treacy, J. M. Gibson, A. Howie, Phil. Mag. A51, 389 (1985).

[5] L. De Caro, A. Giuffrida, E. Carlino, L. Tapfer, Acta Cryst. A53, 1 (1997).

[6] S. J. Pennycook, D. E. Jesson, Phys. Rev. Lett. 64, 938 (1990).

[7] S. J. Pennycook, in "Advances in imaging and electron physics" vol. 123 Academic Press (2002).

[8] E. Carlino, S. Modesti, D. Furlanetto, M. Piccin, S. Rubini, A. Franciosi, Appl. Phys. Lett. 83, 662 (2003).

[9] Y. F. Yanfa, M. M. Al-Jassim, M. F. Chisholm, L. A. Boatner, S. J. Pennycook, M. Oxley, Phys. Rev. B 71, 041309 (2005).

[10] E. Carlino, V. Grillo, Phys. Rev. B. 71 235303 (2005).

[11] P. D. Nellist, S. J. Pennycook, Jour. Microsc. 190, 159 (1998).

[12] B. Rafferty, S. J. Pennycook, Ultramicroscopy 78, 141-151 (1999).

[13] P. D. Nellist, M. F. Chisholm, N. Dellby, O. L. Krivanek, M. F. Murfitt, Z. S. Szilagyi, A. R. Lupini, A. Borisevich, W. H. Sides jr., S. J. Pennycook, Science 305, 1741 (2004).

[14] M. M. J. Treacy, A. Howie, S. J. Pennycook, Inst. Phys. Conf. Ser. 52, 261 (1980).

[15] B. F. Buxton, S. J. Loveluck, J. W. Steeds, Phil. Mag. 38, 259 (1978).

[16] O. Scherzer, Jour. Appl. Phys. 20, 20 (1949).

[17] S. J. Pennycook, D. E. Jesson, P. D. Nellist, M. F. Chisholm, N. D. Browning, in "Handbook of microscopy" VCH publishers, Weinheim, Germany, 595, (1997).

[18] P. Hirsh, A. Howie, R. B. Nicholson, D. W. Pashley, M. J. Whelan, "Electron Microscopy of thin crystals" Krieger publ. C. 2nd Ed. 1977.

[19] E. M. James, N. D. Browning, Ultramicroscopy 78, 125 (1999).

[20] E. Carlino, V. Grillo, Proceedings MCEM VII Portoroze (Si) June 2005 p 159 ISBN 961-6303-69-4.

[21] A. Colli, E. Carlino, E. Pelucchi, V. Grillo, A. Franciosi, J. Appl. Phys. 96 (5) p. 2592 (2004).

[22] S. C. Anderson, C. R. Birkeland, G. R. Anstis, D. J. H. Cockayne, Ultramicroscopy 69, 83 (1997).

[23] K. Ishizuka, Ultramicroscopy 90, 71 (2002).

[24] E. J. Kirkland, Advanced Computing in electron microscopy, p. 100 plenum NewYork (1998).

[25] P. D. Nellist, S. J. Pennycook, Ultramicroscopy 76, 111 (1999).

[26] K. Watanabe, T. Yamazaki, I. Hashimoto, M. Shiojiri, Phys.Rev. B 64, 115432 (2001).

[27] L. J. Allen, S. D. Findlay, M. P. Oxley, C. J. Rossouw, Ultramicroscopy 96, 47 (2003).

[28] Y. Peng, P. D. Nellist, S. J. Pennycook, J. Electron Microscopy 53, 257 (2004).

[29] R. F. Loane, P. Xu, J. Silcox, ActaCryst. A47, 267 (1991).

[30] T. Yamazaki, K. Watanabe, A. Recnik, M. Ceh, M. Kawasaki, M. Shojiri, J.Electron. Micros. 49, 753 (2000).

[31] G. R. Anstis, S. C. Anderson, C. R. Birkenland, D. J. H. Cockayne, Scanning Microscopy 11, 287 (1997).

[32] C. Dwyer, J. Etheridge, Ultramicroscopy 96, 343 (2003).

[33] http://www-unix.mcs.anl.gov/mpi/mpich and references therein.

[34] V. Grillo, P. Verecchia, V. Rosato, E. Carlino, Proceedings MCEM VII Portoroze (Si) p 163 ISBN 961-6303-69-4 (2005).

[35] V. Grillo, P. Verecchia, V. Rosato, E. Carlino, to be submitted to Ultramic.

[36] E. Carlino, V. Grillo, to be submitted.

[37] K. Watanabe, Y. Kotaka, N. Nakanishi, T. Yamazaki, I. Hashimoto, M. Shiojiri, Ultramicroscopy 92, 191 (2002).

[38] T. Yamazaki, N. Nakanishi, A. Recnik, M. Kawasaki, K. Watanabe, M. Ceh, M. Shojiri, Ultramicroscopy 98, 305 (2004).

[39] P. M. Voiles, J. L. Grazul, D. A. Muller, Ultramicroscopy 96, 251 (2003).

[40] J. Silcox, P. Xu, R. F. Loane, Ultramicroscopy 47, 173 (1992).

[41] V. Grillo, E. Carlino, submitted to Ultramicroscopy.